Acta Cryst. (1997). B53, 221–230

Rutile Superstructure of $Sb_{0.9}V_{1.1}O_4$

ANGEL R. LANDA-CÁNOVAS,[a]*† STAFFAN HANSEN[b] AND KENNY STÅHL[c]

[a]*Departamento de Química Inorgánica, Facultad de Ciencias Químicas, Universidad Complutense de Madrid, 28040 Madrid, Spain,* [b]*National Center for HREM, Inorganic Chemistry 2, Chemical Center, University of Lund, PO Box 124, S-221 00 Lund, Sweden, and* [c]*Chemistry Department, Bygning 207, Technical University of Denmark, DK-2800 Lyngby, Denmark. E-mail: bloody@eucmax.sim.ucm.es*

(Received 23 April 1996; accepted 17 October 1996)

Abstract

The structure of $Sb_{0.9}V_{1.1}O_4$, antimony vanadium oxide, has been studied by powder X-ray diffraction, electron diffraction and high-resolution electron microscopy (HREM). The X-ray powder diffraction pattern showed only basic rutile reflections [a_r = 4.6085 (1), c_r = 3.0867 (1) Å] and the basic rutile structure was refined using the Rietveld method. A rutile superstructure was revealed when the sample was studied by electron diffraction. The electron diffraction patterns were indexed on the unit cell $a = 2^{1/2}a_r$, $b = 2^{1/2}b_r$, $c = 2c_r$. Its space group, $I4_1md$, was determined by means of convergent-beam electron diffraction (CBED). A structural model based on alternating cation ordering along **c** in the chains of edge-sharing octahedra is proposed and its electron diffraction patterns and HREM image are calculated and matched with the experimental ones.

1. Introduction

The rutile crystal structure was determined by Vegard (1916). It is an AX_2-type structure and can be described as rows of edge-sharing AX_6 octahedra along the z-direction joined by corner sharing in the xy plane. Baur (1994) lists 16 structure types derived from the aristotypic rutile structure. From these, only two – $CuUO_4$ and trirutile – are formed by cation ordering along the chains of edge-sharing octahedra.

In a recent work two non-stoichiometric series have been described for $\approx SbVO_4$ (Landa-Cánovas, Nilsson, Hansen, Ståhl & Andersson, 1995). This compound, with rutile-type structure, is used as part of a catalyst in a recently developed method for the direct production of acrylonitrile by the ammoxidation of propane. The two non-stoichiometric series described are $Sb_{0.9}V_{0.9+x}\square_{0.2-x}O_4$, $0 \le x \le 0.2$, and $Sb_{0.9-y}V_{1.1+y}O_4$, $0 \le y \le 0.7$. Both series have a common end-member, $Sb_{0.9}V_{1.1}O_4$, which shows by electron diffraction, but not by powder X-ray diffraction, superlattice reflections characteristic of a $2^{1/2} \times 2^{1/2} \times 2$, *i.e.* fourfold, rutile superstructure. We have so far only been able to prepare $Sb_{0.9}V_{1.1}O_4$ in the presence of excess α-Sb_2O_4, due to the volatility of antimony oxide at high temperature and low oxygen partial pressure.

Magnetic susceptibility measurements (Schüer & Klemm, 1973), Mössbauer spectroscopy (Birchall & Sleight, 1976), ESR (Berry & Brett, 1983), bond-valence summations (Hansen, Ståhl, Nilsson & Andersson, 1993) and energy-dispersive X-ray spectroscopy (EDX) experiments (Landa-Cánovas, Nilsson, Hansen, Ståhl & Andersson, 1995) revealed that only Sb^{5+}, V^{4+} and V^{3+} were present and characterized the composition of the end-member studied here as $Sb_{0.92\,(1)}V_{1.08\,(1)}O_4$ (EDX). The unit cell and symmetry observed by electron diffraction in this compound do not fit with any of the 16 different types described by Baur (1994). The purpose of this paper is the elucidation and description of the crystal structure of the rutile-type superstructure observed in $Sb_{0.9}V_{1.1}O_4$.

2. Experimental

2.1. *Synthesis*

An equimolar mixture of V_2O_5 (Riedel–de Haën, 99.5%) and Sb_2O_3 (Merck, > 99%) was heated at 1073 K in a silica ship, inside a silica tube, under flowing N_2 (Aga Plus, < 5 ppm O_2 and < 5 ppm H_2O). Oxygen was removed from the gas flow by passing the nitrogen through a several centimetres long skein of thin copper wire, which was placed in front of the ship in the furnace. Due to the presence of Cu metal at the end of the experiment, the oxygen pressure is assumed to be below the equilibrium pressure over a Cu/Cu_2O mixture, *i.e.* $\le 10^{-11}$ atm.

2.2. *X-ray diffraction*

The sample was studied by X-ray powder diffraction using a Guinier–Hägg camera with Cu $K\alpha_1$ radiation (λ = 1.54056 Å) and Si (a = 5.43088 Å) as an internal standard. Additional runs were performed using an INEL diffractometer, with CPS 120 detector and Cu $K\alpha_1$ radiation in transmission mode. X-ray powder intensity data were collected in reflection mode on a Huber single

† Present address: Centro de Microscopía Electrónica Luis Bru, FCC Químicas, Universidad Complutense de Madrid, 28040 Madrid, Spain.

crystal diffractometer, equipped with a spinning powder sample holder and Mo $K\alpha_{1-2}$ radiation (λ = 0.70932 and 0.71359 Å).

2.3. *Electron microscopy*

Electron diffraction was carried out on a transmission electron microscope (JEM 2000FX) fitted with an EDX detector and a LINK AN10000 system. For CBED experiments a Gatan double-tilt liquid-nitrogen cooling holder was used. HREM was performed in a JEM 4000EX electron microscope (400 kV) with a structural resolution of 1.6 Å. Image simulations were made with the computer program *NCEMSS* (Kilaas, 1987) using the multislice method. Kinematical selected-area electron diffraction (SAED) patterns were calculated with the *EMS* (Stadelman, 1987) simulation program. For image processing, the *Semper-Plus* 6 (Saxton, 1978) program was used.

3. Results

3.1. *X-ray structure refinements*

The powder X-ray-diffraction patterns recorded in three different types of experiments showed only basic rutile and α-Sb_2O_4 reflections. Therefore, only the basic rutile structure could be refined by means of Rietveld analyses. The molybdenum data were utilized for this purpose and the program used, *LHMP*1 (Hill & Howard, 1986), was modified to allow for split pseudo-Voigt profile functions instead of conventional asymmetry corrections and Chebyshev functions for background modelling. Orthorhombic α-Sb_2O_4 was introduced as a second phase without attempting to refine its structure (Thornton, 1977).

The refined parameters comprised ten profile parameters, nine background parameters, one 2θ–zero parameter, two scale factors, two plus three unit-cell parameters and eight structural (coordinate, occupancy and anisotropic temperature factors) parameters for $\approx SbVO_4$. The scattering factors were taken as equal mixtures of Sb^0–Sb^{5+}, V^0–V^{3+} and O^0–O^{2-}, following the findings by Matsuhata, Gjønnes & Taftø (1994), and were taken from *International Tables for Crystallography* (1992, Vol. C) and for O^{2-} from Hovestreydt (1983). The refinements were considered converged when the maximum shift/parameter e.s.d. was less than 0.2. The α-Sb_2O_4/$SbVO_4$ scale factor ratio was found to be 0.5%. In Fig. 1 the experimental diffraction pattern and the difference between the experimental and calculated ones are presented. The refinement results are summarized in Table 1.*

* The numbered intensity of each measured point on the profile has been deposited with the IUCr (Reference: AB0356). Copies may be obtained through The Managing Editor, International Union of Crystallography, 5 Abbey Square, Chester CH1 2HU, England.

Table 1. *Rietveld refinement summary*

2θ range (°)	12.00–90.00
Step size (°)	0.02
No. of profile steps (n)	3900
No. of Bragg reflections	168
No. of parameters (p)	36
$R_p = \Sigma\lvert Y_i^o - Y_i^c\rvert/\Sigma(Y_i^o)$ (%)	5.79
$R_{wp} = \{\Sigma w_i(Y_i^o - Y_i^c)^2/\Sigma(w_i Y_i^{o2})\}^{1/2}$ (%)	7.86
GOF $= \Sigma w_i(Y_i^o - Y_i^c)^2/(n-p)$	2.93
$R_{\text{Bragg}} = \Sigma\lvert I_k^o - I_k^c\rvert/\Sigma(I_k^o)$ (%)	1.78
Space group	$P4_2/mnm$
a (Å)	4.6085 (1)
c (Å)	3.0867 (1)
x(O)	0.3040 (4)
B_{av}(Sb/V) (Å^2)	0.70 (2)
B_{av}(O) (Å^2)	0.77 (9)
Refined composition	$Sb_{0.92(1)}V_{1.08(1)}O_4$

3.2. *Selected-area electron diffraction*

Although superlattice reflections are present over a small range in both non-stoichiometric series mentioned previously, they were always more intense in the end-member. Consequently, most of the electron diffraction study has been carried out on this type of sample.

The reciprocal lattice of $Sb_{0.9}V_{1.1}O_4$ has been studied by SAED. Fig. 2 shows four high-symmetry SAED patterns. It is very important to notice that although most SAED patterns show superlattice reflections, no extra reflections are observed when the SAED pattern is obtained along [001]. Another interesting fact is that the superstructure reflections were always more intense in the $[101]_r \equiv [111]^*$ diffraction patterns.

A careful reciprocal lattice study by electron diffraction has revealed the following unit cell for the rutile superstructure $a = 2^{1/2}a_r$, $b = 2^{1/2}a_r$ and $c = 2c_r$.

All reflections hkl, $h + k + l = 2n + 1$, are systematically absent, according to the extinction conditions for a body-centred unit cell. The high multiple-diffraction

* Subindex r refers to the basic rutile unit cell. Directions, planes *etc.* given without subindices always refer to the supercell.

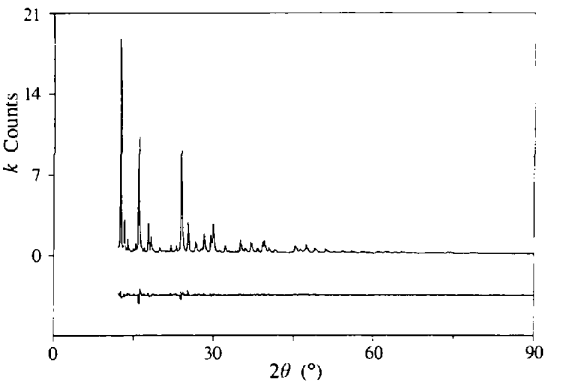

Fig. 1. Powder X-ray diffraction profile (Mo $K\alpha$) of $Sb_{0.9}V_{1.1}O_4$ and α-Sb_2O_4. The final calculated difference pattern is shown below the experimental.

character of electron scattering does not affect the body-centred forbidden reflections, since there is no allowed vector in the reciprocal lattice that can add intensity to them.

The transformation matrix from the rutile cell to the supercell is

$$M = \begin{bmatrix} 1 & 1 & 0 \\ -1 & 1 & 0 \\ 0 & 0 & 2 \end{bmatrix}.$$

3.3. *Convergent-beam electron diffraction*

CBED experiments were difficult to perform since the superlattice ordering usually did not cover large areas in the crystal. However, occasionally the crystals presented a very high degree of order that allowed recording of good enough quality CBED patterns.

In Fig. 3(*a*) a CBED pattern along the [001] direction is shown. It can be seen that superlattice reflections are observed in the first-order Laue zone (FOLZ), but not in the zero-order Laue zone (ZOLZ) or the second-order Laue zone (SOLZ). The pattern shows 4*mm* whole pattern (WP) symmetry, *i.e.* the two-dimensional point-group symmetry observed in the whole pattern, see Buxton, Eades, Steeds & Rackham (1976). In Fig. 3(*b*) a blow up of the ZOLZ reveals the presence of Gjønnes–Moodie (G–M) lines for *hh*0 and *hh̄*0 (*h* odd) reflections, which are indicative of a *d* glide plane parallel to <110> (Buxton, Eades, Steeds & Rackham, 1976; Tanaka & Terauchi, 1985). In Fig. 4 a CBED pattern along the [010] ≡ $[110]_r$ direction shows the presence of a mirror plane perpendicular to **a***. Careful examination of the diagrams in Figs. 3(*a*) and 4 demonstrates a shift between the ZOLZ and the

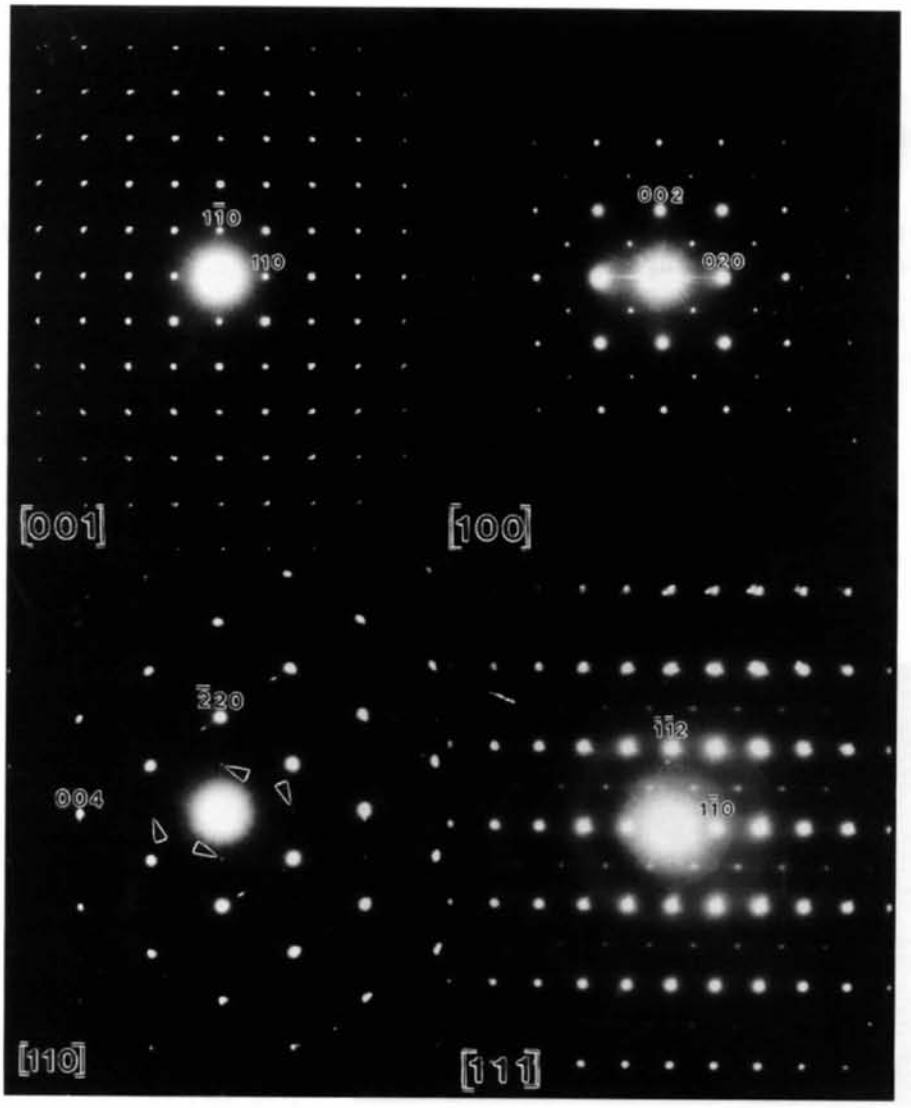

Fig. 2. SAED patterns from different $Sb_{0.9}V_{1.1}O_4$ crystals along four high-symmetry directions. Notice the absence of superlattice reflections in the [001] zone-axis pattern and their weakness along [110].

Table 2. *Scheme of the procedure followed for the rutile superstructure space-group determination by CBED (see text for explanation)*

Point-group determination

	WP symmetry	Diffraction group	Point group
• [001]	$4m_v m_v$	$4mm$	$4mm$
		$4mm1_R$	$4/mmm$
			$m3m$ (Cubic)

	WP symmetry
• ⟨100⟩	m_v

Point group	Diffraction group	WP symmetry
$4mm$	$m1_R$	m_v
$4/mmm$	$2mm1_R$	$2m_v m_v$

Point group: $4mm$

Space group determination

- Lattice type

$[001] \Rightarrow hk0 : h + k = 2n$
$hk1 : h + k = 2n + 1$ $\quad h + k + l = 2n$
$\langle 100 \rangle \Rightarrow 0kl : k + l = 2n$ $\quad \Downarrow$
$1kl : k + l = 2n + 1$ $\quad I$ centring

- G–M lines

$[001] \Rightarrow hh0, h = 2n + 1 \quad \Rightarrow I\_\_d$
$h\bar{h}0, h = 2n + 1$
$[h01] \Rightarrow$ no G–M lines $\quad \Rightarrow I4_1md$
$h, l = 2n + 1 \quad \Rightarrow I\bar{4}_1cd$

FOLZ reflection nets, which is characteristic for a body-centred cell. The lack of a difference in periodicity between the ZOLZ and the FOLZ indicates the absence of a glide plane perpendicular to this direction.

In Table 2 we summarized the procedure followed to determine the superlattice space group. The $4mm$ WP symmetry observed in the [001] CBED pattern allows only two possible diffraction groups, which correspond, along this direction, to three possible point groups. The third point group is rejected because it is possible only for cubic symmetries. The presence of only one mirror plane in the <100> CBED pattern, *i.e.* the absence of a mirror plane perpendicular to **c***, eliminates the $4/mmm$ point group and confirms the $4mm$ point group for this rutile superstructure.

Table 3. *Possible ways of arranging four chains of edge-sharing octahedra along* **c** *with ABAB metal ordering in rutile*

No.	Type*	Maximum symmetry	Unit cell
1	*AA*	*Pmmn*	$a_1 = 2^{1/2}a_r$
	AB		$b_1 = 2^{1/2}b_r$
			$c_1 = 2c_r$
2	*AB*	$I4_1md$	$a_2 = 2^{1/2}a_r$
	AB		$c_2 = 2c_r$
3	*AB*	$P\bar{4}2_1m$	$a_3 = a_r$
	BA		$c_3 = 2c_r$
4	*AA*	≡ no. 3	
	AA		

* Ordering in the *ab* plane.

When the observed body-centring, $4mm$ point group and the *d* glide plane are considered, only two possible space groups are allowed, $I4_1md$ and $I4_1cd$. The presence of a *c* glide plane can be excluded from the [100] zone-axis pattern, see Fig. 2(*b*), since we observe $0kl$, $l = 2n + 1$, reflections and in this zone axis there is no possibility of double diffraction phenomena that could add intensity to them. Therefore, we deduce the space group $I4_1md$ for the observed superlattice.

3.4. *Superstructure model*

To find a suitable model that explains the electron diffraction patterns observed, we considered the fact that in the electron diffraction pattern along the [001] direction no superlattice spot was observed in the ZOLZ, suggesting that it is some type of ordering along the edge-sharing octahedral chains that produces the superstructure and, therefore, the projection of the structure along [001] will not show any indication of extra ordering. This, together with the presence of almost

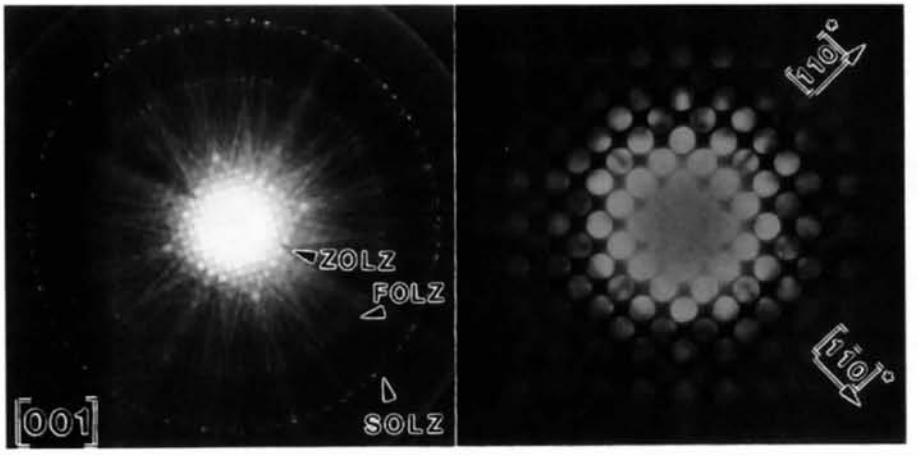

Fig. 3. (*a*) CBED pattern along the [001] direction. Zero-, first- and second-order Laue zones are indicated. (*b*) Central area of Fig. 2(*a*). Notice the G–M lines along [110]* and [1$\bar{1}$0]*.

Table 4. *Crystallographic data for the structural model proposed for the $Sb_{0.9}V_{1.1}O_4$ rutile superstructure*

Space group $I4_1md$, unit-cell parameters: $a = 2^{1/2}a_r$, $b = 2^{1/2}b_r$, $c = 2c_r$ [$\mathbf{a}_r = 4.6085(1)$, $\mathbf{c}_r = 3.0867(1)$ Å].

Wyckoff position*	Positional coordinates			Atomic occupancy
	x	y	z	
(4*a*)	0.0	0.0	0.0	V
(4*a*)	0.0	0.0	0.5	Sb
(8*b*)	0.0	0.304	0.0	O(1)
(8*b*)	0.0	0.696	0.5	O(2)

* (4*a*) $0,0,z$; $0,\frac{1}{2},z+\frac{1}{4}$; (8*b*) $0,y,z$; $\frac{1}{2},\frac{1}{2}-y,z+\frac{1}{2}$; $-y,\frac{1}{2},z+\frac{1}{4}$; $y+\frac{1}{2},0,z+\frac{3}{4}$.

equal amounts of two different cations, led us to use as a starting assumption that the ordering of the two different cations along the [001] direction produces the superlattice.

We tested all the possible models for alternating cation ordering along the c direction and only one could be found that fitted with a $2^{1/2}a_r$, $2^{1/2}b_r$, $2c_r$ body-centred unit cell, see Table 3. This structure model is represented in Fig. 5 and its ideal atomic coordinates in Table 4. The model is consistent with the $I4_1md$ space group, also agreeing with the symmetry detected by CBED.

3.5. *High-resolution electron microscopy*

HREM experiments presented large difficulties, probably because of the tendency of the $Sb_{0.9}V_{1.1}O_4$ crystals to lose antimony oxide, as previously reported by Berry, Brett & Patterson (1983) and Landa-Cánovas, Nilsson, Hansen, Ståhl & Andersson (1995). This tendency seems to increase with the higher vacuum obtained in the HREM microscope. Thus, while in a 2000 FX microscope the crystals show clear superlattice reflections, in the 4000EX microscope these reflections smear out and cause diffuse intensity lines parallel to [110]* (Fig. 6)

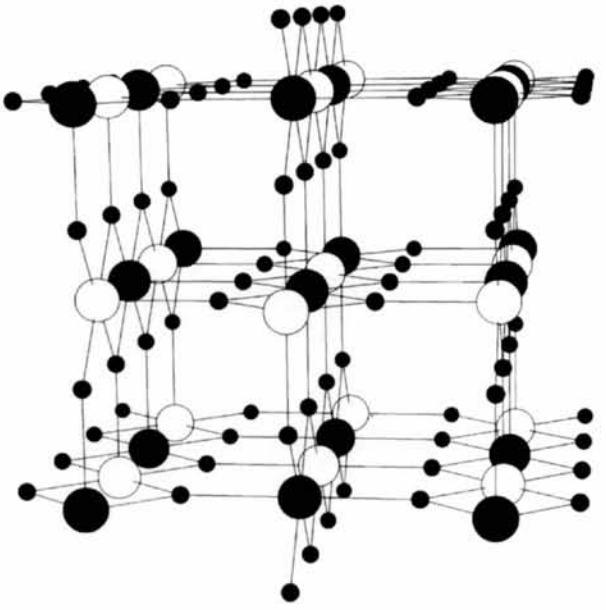

Fig. 5. Structure model proposed for the rutile superstructure observed in $Sb_{0.9}V_{1.1}O_4$ seen approximately along **c**. Large black spheres denote Sb atoms, large open spheres V atoms and small open spheres O atoms.

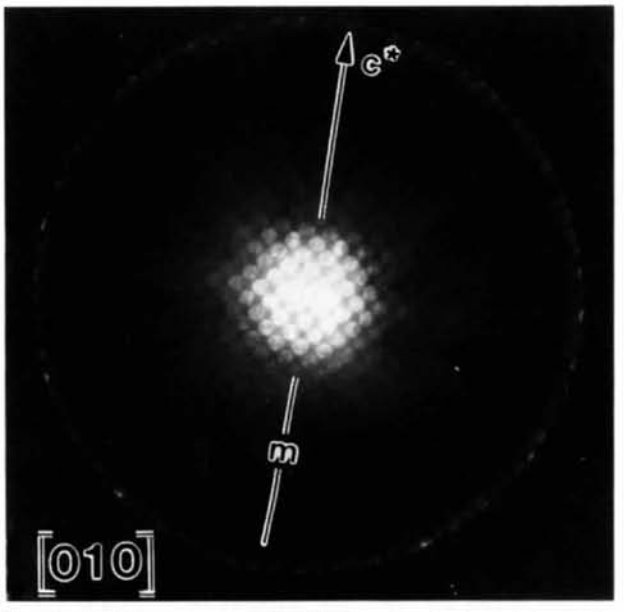

Fig. 4. CBED pattern of an $Sb_{0.9}V_{1.1}O_4$ crystal oriented along the [010] direction. A mirror plane perpendicular to **a*** is indicated.

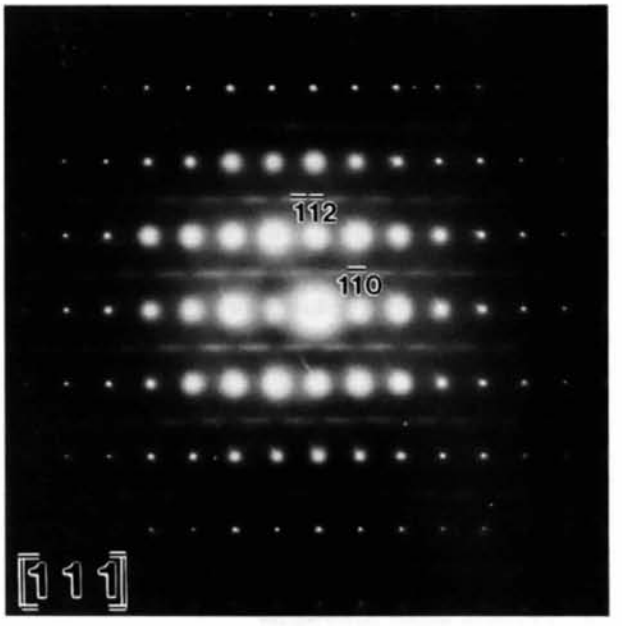

Fig. 6. Electron diffraction pattern from a $Sb_{0.9}V_{1.1}O_4$ crystal oriented along the $[101]_r \equiv [111]$ direction recorded on a JEM 4000EX electron microscope, *cf.* the equivalent diffraction pattern in Fig. 2.

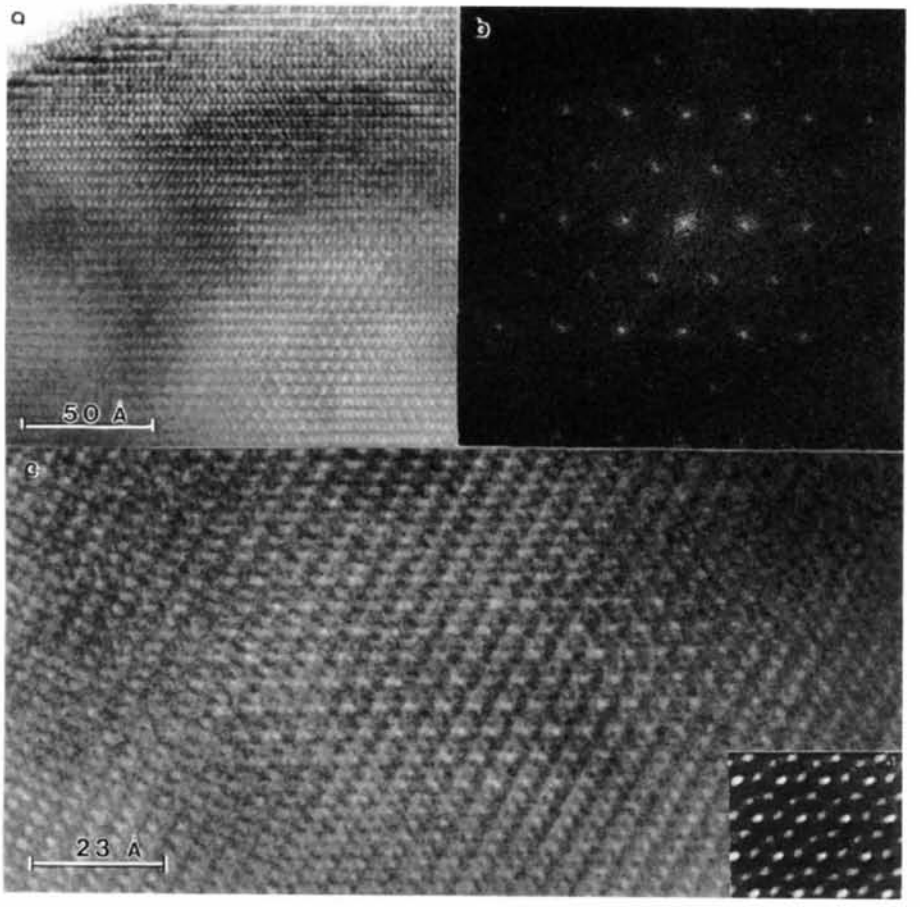

Fig. 7. (*a*) High-resolution micrograph from a $Sb_{0.9}V_{1.1}O_4$ crystal along the [111] direction. (*b*) Fourier transform of one superstructure domain (*Semper-Plus* 6; Saxton, 1978), showing the presence of well defined superlattice reflections. (*c*) Magnified illustration of a superstructure domain in Fig. 7(*a*). The image simulation is inserted in the lower right corner (crystal thickness 100 Å, defocus 350 Å).

as we observed in samples with composition near the existence limit of this rutile superstructure, *cf.* Fig. 2 in Landa-Cánovas, Nilsson, Hansen, Ståhl & Andersson (1995).

However, high-resolution images could nevertheless be obtained. In these the superstructure was present in small islands in a rutile-type matrix (Fig. 7). Image simulations of the proposed structural model fit with the experimental image. The image was recorded along the $[101]_r$ direction, because it is along this direction which the superstructure reflections show higher intensity. The model projection of Fig. 8 shows that along this direction all the cations of each species are aligned perfectly in rows along the viewing direction, explaining why the superlattice reflections are more intense in this zone axis.

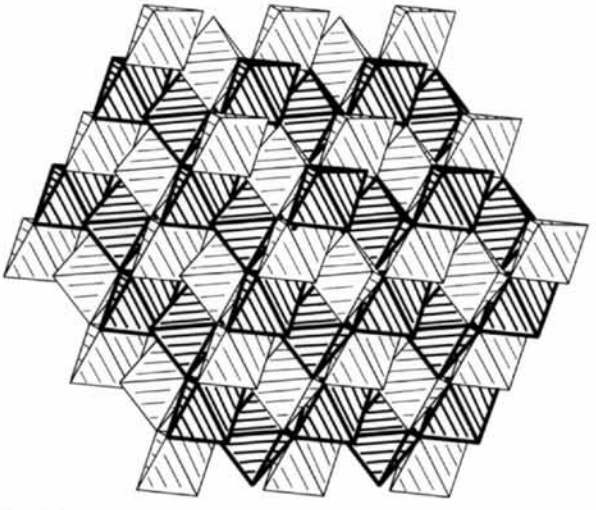

Fig. 8. Projection of the proposed model along the [111] direction. The centres of dark and light shaded octahedra are occupied by V and Sb cations, respectively. The corners of the octahedra are occupied by oxygen anions.

4. Discussion

4.1. *Structure model description*

This model can alternatively be interpreted as two interpenetrating cation spirals running along **c** in the

rutile-type anion sublattice, each spiral formed by one type of cation. Another way to describe this structure is as a topological transformation of the zircon structure-type (see Fig. 9). In the zircon-type structure the big cation occupies the bisdisphenoids (eight-cornered polyhedra) and the small cation occupies the tetrahedral polyhedra. Both polyhedra share edges and the whole structure transforms into the described rutile superstructure by a slight shift of the cations and anions in two edge-sharing octahedra, as shown by Hyde & Andersson (1989). In other words, the structure presents the same cation arrangement as the zircon-type structure, but the cations are not displaced from the centre of the octahedra. However, we must point out that the electron diffraction and the X-ray powder diffraction show that almost no distortion is present in the basic rutile sublattice. Besides, the zircon structure-type presents an *a* glide plane perpendicular to **c**, which is not possible when the rutile-type anion sublattice is kept unaltered. In the $Sb_{0.9}V_{1.1}O_4$ superstructure, CBED experiments have shown the absence of such an *a* glide plane.

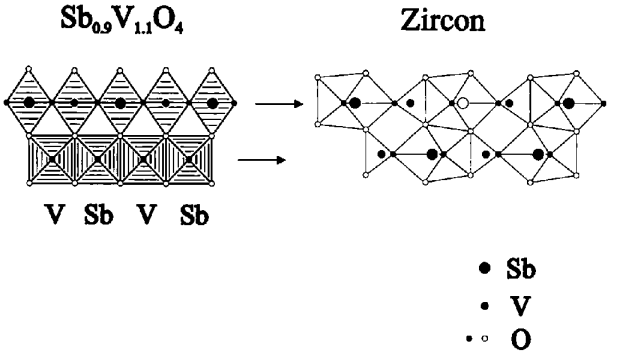

Fig. 9. Layers of the described rutile superstructure and zircon-type structure (modified from Hyde & Andersson, 1989).

The electron diffraction patterns for this model were calculated in the kinematical case with the EMS computer program (Stadelman, 1987). In Fig. 10 we show the calculated patterns corresponding to the four directions shown in Fig. 2. The fitting is excellent. Although this fitting is not quantified as in X-ray diffraction, it shows that at least qualitatively the model is correct.

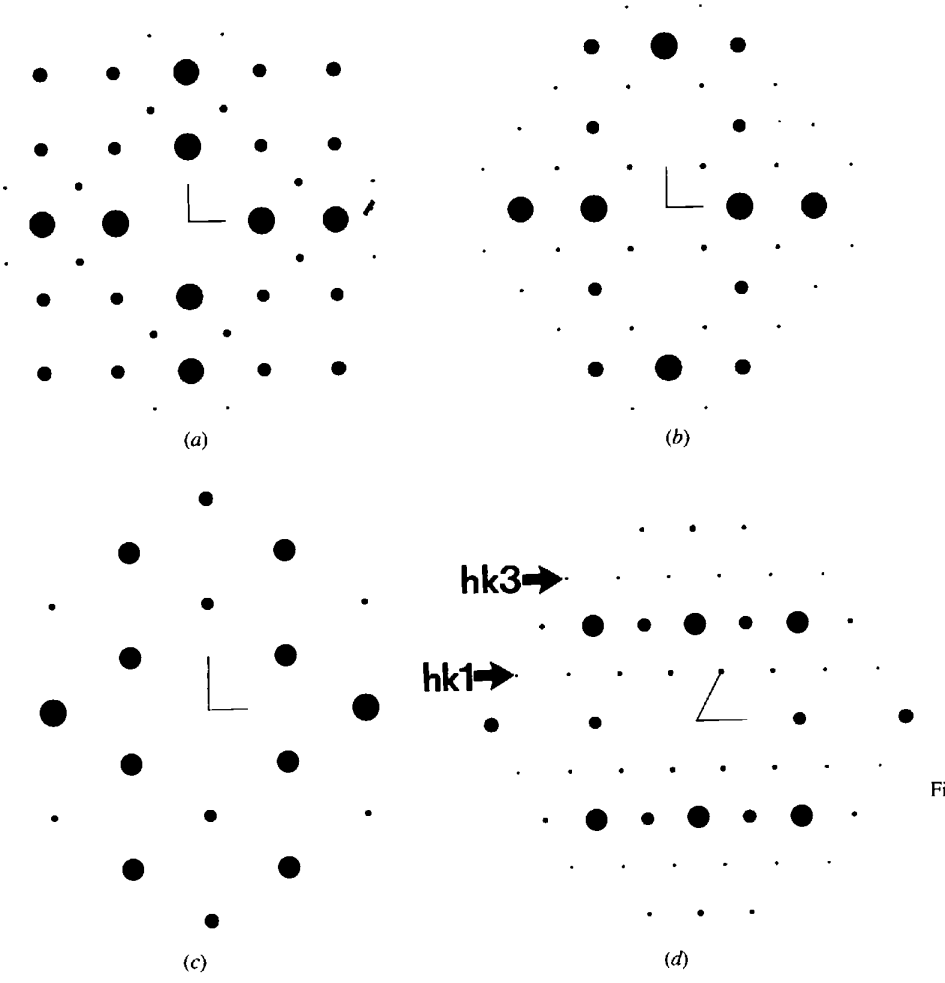

Fig. 10. Calculated SAED patterns, oriented as in Fig. 2, for the fully ordered $Sb_{0.9}V_{1.1}O_4$ rutile superstructure model proposed along the directions: (*a*) [001], (*b*) [100], (*c*) [110] and (*d*) [111], respectively, using the kinematical approximation.

4.2. *Compositional versus displacive model*

The possibility of a displacive superstructure remains to be commented upon. The observed space group only allows cation displacements along the *c* axis, because the cations lie in the intersection between two mirror planes. Therefore, only longitudinal displacements along the *c* axis are possible. In that case the superstructure will be formed by a coupling of the atoms along the [001] direction. It is well known (Korekawa, 1967) that in compositionally modulated structures the intensity of the modulation reflections will vary in the same way as the intensities of the basic reflection intensities all along the diffraction pattern, but if the modulation is of longitudinal displacive character along *z*, the intensity of the modulation reflections will increase, if compared with the basic ones, as the *l* Miller index of the reflections increases. A physically reasonable displacive model is obtained with the positional coordinates set to $z = 0.02$ for the first metal position and $z = 0.48$ for the second, and a fully disordered cation distribution. The cations thus become slightly more off-centre in the octahedra with metal–oxygen distances of 1.91 (2×), 1.99 (2×) and 2.10 Å (2×), for both sites. In the model without metal-atom displacements (Table 4), the distances are 1.98 (2×) and 2.00 Å (4×). The metal–metal distances along **c** in the displacive model become alternatingly 2.84 and 3.33 Å. In the model without displacements the corresponding metal–metal distances are all equal to 3.09 Å. This can be compared with the situation in monoclinic V_2O_4 (Longo & Kierkegaard, 1970), where alternating V—V distances of 2.62 and 3.18 Å (average 2.90 Å) were observed. For the displacive model of $Sb_{0.9}V_{1.1}O_4$, the electron diffraction patterns have been calculated and are shown in Fig. 11. A distinctive characteristic is found in the [111] zone axis, where the *hk*3 reflection row (marked with an arrow) shows a higher intensity than the *hk*1 row, while in the compositional model and in the experimental case higher intensity is observed in the *hk*1 row than in the *hk*3 row. The dynamical character of electron scattering may cause a

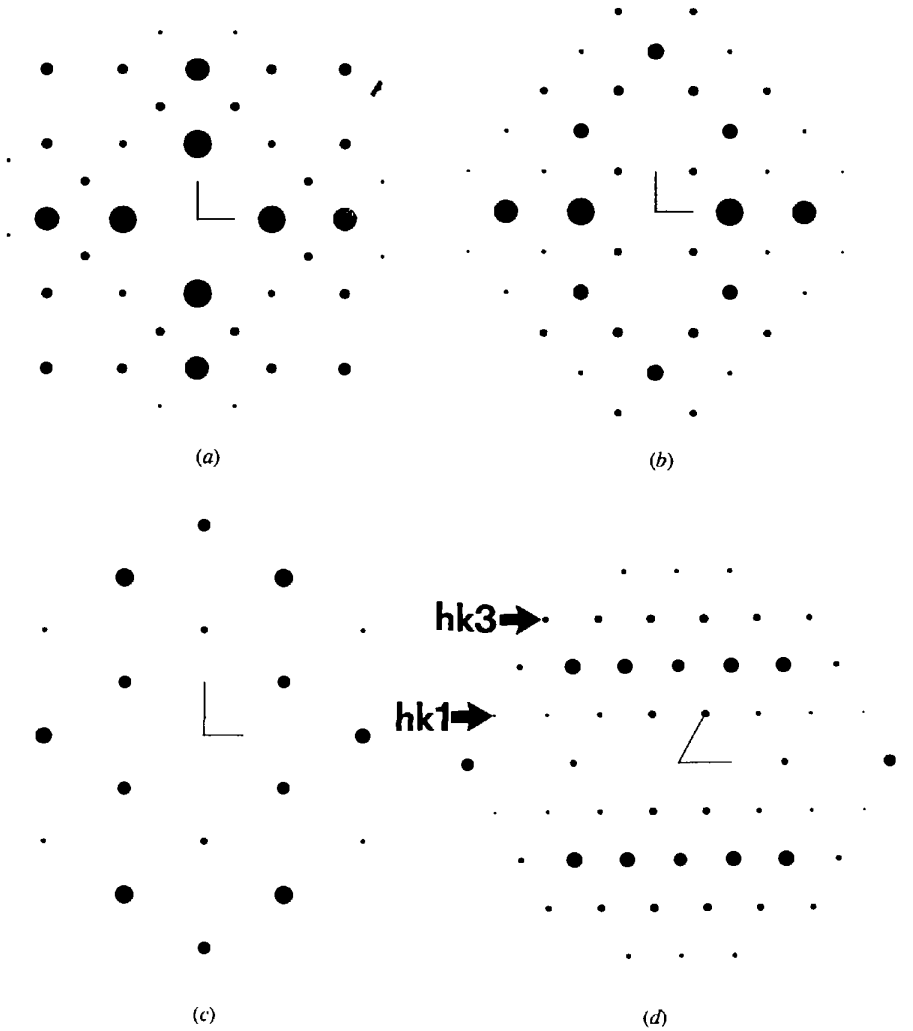

Fig. 11. Calculated SAED patterns equivalent to Fig. 10 for a displacive superstructure model with cation displacement along the *c* axis, but with a fully disordered distribution of Sb and V.

tendency to level the intensity of both rows, but never to invert their respective intensities. Since dynamical scattering affects much less superstructure reflections due to their relative weak intensity, the calculated kinematical intensities for superstructure reflections can successfully be compared with the experimental ones while, as can be seen in Figs. 2, 10 and 11, the average structure reflections are strongly affected by dynamical scattering.

In Fig. 2(*b*) it can be seen that the reflections *hhl*, $2h + l = 2n$, are extremely weak, but present, breaking the reflection condition imposed by the *d* glide plane (*hhl*, $2h + l = 4n$). These reflections show Gjønnes–Moodie lines in CBED patterns, whose presence can only be explained by double diffraction phenomena from the FOLZ, as is well known in the case of *d* glide-forbidden reflections in spinel.

A displacement of the anions along the *ac* and *bc* planes is also possible either expanding or contracting the octahedra, allowing them to adapt to the different cation sizes, which is important from the chemical point of view. This would have very little effect on the electron diffraction pattern and it has not been possible for us to observe it.

4.3. *Rietveld calculations*

The electron diffractograms exhibit a rutile superstructure not detected in the powder X-ray diffraction experiments, performed using Mo $K\alpha$ radiation in reflection mode or monochromatic Cu $K\alpha_1$ radiation in transmission mode. Powder diffraction spectra calculated for the superstructure model with different degrees of metal ordering (and metal-atom displacements) allow us to conclude that the average metal ordering in the samples must be far from perfect. However, it turns out to be difficult to estimate an upper limit for the degree of ordering that should be detectable considering the noise level in the experimental spectra. This is due to an almost perfect overlap of the two strongest (lowest theta) superlattice reflections of $Sb_{0.9}V_{1.1}O_4$ with reflections from α-Sb_2O_4. As mentioned before, we have not been able to prepare samples of $Sb_{0.9}V_{1.1}O_4$ without α-Sb_2O_4 being present, when working in an open system.

The observation by X-rays of considerable average disorder is nevertheless compatible with the electron microscopy results, which indicate the presence of small domains of relatively ordered structure in the crystals, *cf.* Fig 7. The minute size, tens of nanometers, of these ordered domains can be expected to broaden the weak superlattice reflections until they are not detectable by powder X-ray diffraction methods.

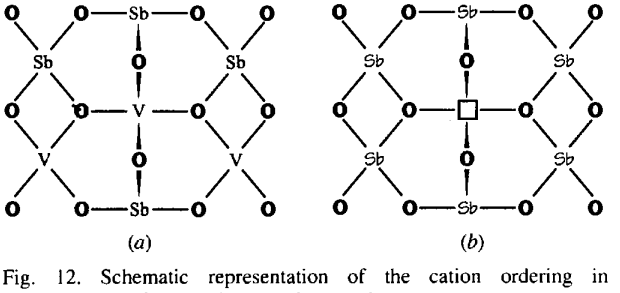

Fig. 12. Schematic representation of the cation ordering in (*a*) $Sb_{0.9}V_{1.1}O_4$ and (*b*) around a metal vacancy.

4.4. *Crystal chemistry*

Recently, we have shown (Landa-Cánovas, Nilsson, Hansen, Ståhl & Andersson, 1995) that when we change the oxidizing conditions during the sample preparation, a non-stoichiometric series of general formulae $Sb_{0.9}V_{0.9+x}\square_{0.2-x}O_4$, $0 \le x \le 0.2$, is formed. The rutile superstructure studied in this work is the end-member with $x = 0.2$, *i.e.* which forms in pure N_2. However, a paradox seems to exist because the ideal model for this superstructure should be for a cation ratio Sb:V = 1:1, but we observe this superstructure when the Sb:V ratio is 0.9:1.1 and it disappears with a slight increase of the oxidation conditions, *i.e.* when the Sb:V ratio approaches unity. In Hansen, Ståhl, Nilsson & Andersson (1993) the crystal structure of the other end-member $Sb_{0.9}V_{0.9}O_4$ was refined by Rietveld methods. A study of bond-valence sums in this work revealed that the oxygens connected to a vacancy are underbonded and consequently tend to have Sb as the two remaining metal ions. In that way, when a vacancy is introduced it will prefer to be surrounded by Sb cations and the Sb—V ordering is immediately broken, as shown in Fig. 12.

We thank Jerker Nilsson who kindly prepared the samples and the Swedish Natural Science Research Council (NFR) for financial support. We also thank Dr L. C. Otero-Díaz for stimulating discussions.

References

Baur, W. H. (1994). *Z. Kristallogr.* **209**, 143–150.
Berry, F. J. & Brett, M. E. (1983). *Inorg. Chim. Acta*, **76**, L205–L206.
Berry, F. J., Brett, M. E. & Patterson, W. R. (1983). *J. Chem. Soc. Dalton Trans.* pp. 9–12.
Birchall, T. & Sleight, A. W. (1976). *Inorg. Chem.* **15**, 868–870.
Buxton, B. F., Eades, J. A., Steeds, J. W. & Rackham, G. M. (1976). *Philos. Trans. R. Soc. London*, **281**, 171–194.
Hansen, S., Ståhl, K., Nilsson, R. & Andersson, A. (1993). *J. Solid State Chem.* **102**, 340–348.
Hill, R. J. & Howard, C. J. (1986). Australian Atomic Energy Commission (now ANSTO) Report M112, Lucas Heights Research Laboratories, New South Wales, Australia.
Hovestreydt, E. (1983). *Acta Cryst.* A**39**, 268–269.
Hyde, B. G. & Andersson, S. (1989). *Inorganic Crystal Structures*. New York: John Wiley.
Kilaas, R. (1987). Proceedings of the 45th Annual Meeting of EMSA, edited by G. W. Bailey, pp. 66–69. Baltimore.
Korekawa, M. (1967). Habilitationsschrift der Ludwigs–Maximilians–Universität München.

Landa-Cánovas, A. R., Nilsson, J., Hansen, S., Ståhl, K. & Andersson, A. (1995). *J. Solid State Chem.* **116**, 369–377.
Longo, J. M. & Kierkegaard, P. (1970). *Acta Chem. Scand.* **24**, 420–426.
Matsuhata, H., Gjønnes, J. & Taftø, J. (1994). *Acta Cryst.* A**50**, 115–123.
Saxton, W. O. (1978). *Adv. Electron. Electron Phys. Suppl.* 10.
Schüer, H. & Klemm, W. (1973). *Z. Anorg. Allg. Chem.* **395**, 287–290.
Stadelman, P. A. (1987). *Ultramicroscopy*, **21**, 131–146.
Tanaka, M. & Terauchi, M. (1985). *Convergent Beam Electron Diffraction*. Tokyo: JEOL Ltd.
Thornton, G. (1977). *Acta Cryst.* B**33**, 1271–1273.
Vegard, L. (1916). *Philos. Mag.* **32**, 65–96.